Hydrol. Earth Syst. Sci. Discuss., 7, C722–C732, 2010
www.hydrol-earth-syst-sci-discuss.net/7/C722/2010/

Hydrology and Earth System Sciences Discussions

Interactive comment on "Groundwater flow and storage within an alpine meadow-talus complex" *by* A. F. McClymont et al.

A. F. McClymont et al.

alastairmcclymont@gmail.com

Received and published: 1 May 2010

Following are our responses to the points raised by Reviewer 2. Pages, figure and line numbers are for the original manuscript. Some revised figures are attached. Revised figure captions are below.

REVIEWER 2 (O. Sass)

GPR:

1.We have tried migrating the GPR data that crosses the meadow using a constant migration velocity of 0.065 m/ns (representative of the meadow sediments). Unfortunately, the resulting image is of much lower quality than the unmigrated version. This is because many of the diffraction hyperbolas originate from out-of-plane features. In

addition, we have included the following text to justify why we have corrected our cross-sections using the higher velocity for bedrock and talus:

"Finally, each trace was corrected from time to depth using an average velocity determined by analyzing the normal moveout of reflections on several common-midpoint profiles (CMPs) that were recorded over talus and bedrock at the site (0.12 m/ns; red circles in Figure 3a; e.g., Annan, 2005). Velocities within the fine-grained soil layer underlying the meadow are expected to be significantly slower. However, because strong attenuation of electromagnetic waves traveling through this layer prevented us from imaging structures within or beneath the meadow, we consider the average velocity representative of talus and bedrock to be the most appropriate for displaying our depth-corrected GPR cross-sections."

2.We acknowledge that diffractions from small boulders are not exclusive to the meadow in the following revised paragraph:

"We interpret the steep reflections observed on profile GPR1 to be the tails of diffraction hyperbolas that originate from boulders within the small sediment-filled depression beneath the meadow (Figure 4a). They are not apparent beneath locations outside the meadow and we suggest that this is a consequence of both strong attenuation effects beneath the meadow and the laterally varying gain functions we use to scale the GPR traces. Even though similar sized boulders can be expected within the talus rubble, the diffractions they produce probably have small amplitudes relative to the high-amplitude reflections from the underlying bedrock. In contrast, soil that occurs in the very near surface beneath the meadow is moist and probably contains a significant component of conductive clay minerals. As a consequence, the electromagnetic waves are strongly attenuated such that the diffractions from the near-surface boulders have much higher amplitudes than reflections from the underlying bedrock."

We therefore agree that there is no structure to see beneath the meadow. We could leave out the envelope processing step, but it is necessary to enhance the deeper

HESSD

7, C722–C732, 2010

structures in other parts of the cross-sections, where reflections from bedrock laminations can be observed to depths of around 20 m. Note that we have changed the text from "> 20 m" to "up to 20 m".

3.We have reanalyzed our CMP data. We were able to gain some useful new insights on the subsurface velocity structure from one CMP (CMP1). We now incorporate this information in the form of a new figure (Figure 5), which shows the CMP data with a full semblance analysis and in the form of new text:

"Apart from CMP1, most of the CMPs analyzed were located either on talus, bedrock, or the margins of the meadow area (Figure 3a). They yielded velocities of around 0.12 $\pm$ 0.01 m/ns, which are typical for loose debris comprising talus deposits and indurated bedrock material (Annan, 2005; Sass, 2006). Although data from CMP1 are somewhat noisy, analysis of a relatively long-wavelength groundwave arrival phase (Vg1) and a single reflection phase (Vr1) reveals a much slower velocity that is more representative of the moist fine-grained soil layer underlying the meadow (0.065 m/ns; Figure 5). A second groundwave phase (Vg2) with a shorter wavelength and a faster picked velocity of 0.12 m/ns appears to originate at around 50 ns (Figure 5). We interpret Vg2 to result from a subsurface refractor of quartzite bedrock beneath the meadow. By assuming a simple two-layer refraction model with a horizontal interface, we can solve for z, the thickness of the soil layer (Kearey and Brooks, 1991):

z = ti * v1 * v2 / 2 * sqrt{v2^2 – v1^2} (Note that this equation has been reformatted for the plain text version posted in the discussion forum)

where ti is the zero-offset intercept time (50 ns), v1 is the velocity of the soil layer (0.065 m/ns), and v2 is the velocity of the bedrock refractor (0.12 m/ns). Based on our analysis, we calculate that the bedrock beneath CMP1 is no deeper than about 1.9 m."

ERT:

4.We address the reviewer's concerns about the spatially restricted 20-60 kohmm zone

HESSD

7, C722–C732, 2010

under the meadow by including the following sentence:

“Although the bedrock resistivities are much higher beneath the meadow than beneath the talus deposit, we do not interpret a change in bedrock composition and suggest that the high values are a consequence of overfitting the inverted resistivity data in this region.”

Seismic refraction:

5.The two velocity phases we describe were identified on shot gathers and not on the seismic tomogram. To clarify this point, we have included an extra figure showing an example shot gather recorded on the talus (Figure 7) and cite it in the following sentence in section 4.3:

“First arrival picks from shot gathers recorded on the talus show two distinct velocity phases: 1) a slow shallow phase with velocities of around 500 m/s associated with the talus cover and 2) a faster deeper phase with velocities of around 3500 m/s, indicating a change to higher velocity bedrock (e.g. Figure 7).”

In the resulting seismic tomogram, velocities representative of bedrock have a wider range of values (2000-4000 m/s) because of smoothness constraints used to invert the data. We also include the following sentence in section 4.4 to justify why we have not used the seismic data to evaluate the depth to bedrock beneath the meadow:

“Because our seismic velocity tomogram has a coarser resolution than the ERT and GPR images, we do not use it to determine the topography of the bedrock surface under the meadow.”

Nevertheless, the interpretation of bedrock depth determined from the seismic tomogram (2-4 m) is in general agreement with our estimates from the GPR and ERT data (less than 4 m).

Combined interpretation:

HESSD

7, C722–C732, 2010

6.We have reanalyzed our data and, based on the evidence described above, could not find any evidence for a deeper bedrock surface beneath the basin. We have modified slightly some justifications we made in our original interpretation to make this clear. This includes the following text in section 4.4:

"Because the groundwaves on most GPR profiles tended to obscure very shallow reflections and because strong electromagnetic-wave attenuation within the moist, clay-rich soil comprising the basin fill suppresses deeper reflections, we could not image the bedrock topography nor reflections from layering within the bedrock underlying the meadow. Nevertheless, as shown in Figure 6b, the top of the bedrock surface imaged by the ERT data generally coincides with the location of the groundwave arrival as observed on the depth corrected GPR cross-sections. For this reason, we consider the vertical position of the groundwave on the depth-corrected GPR cross-sections to be a crude proxy for the maximum depth to bedrock beneath the meadow. If the bedrock were much deeper, we would expect a to see a coherent reflection produced by the strong electromagnetic contrast produced between the soil layer and bedrock. On the depth-corrected GPR cross-sections, variations in the arrival depth of the groundwave phase provide a qualitative indicator of lateral changes in the depth to bedrock beneath the meadow; where the groundwave phase shallows the bedrock surface must also shallow and, conversely, where the groundwave phase deepens the bedrock must deepen."

Specific comments:

7.Page 1538, line 23. We have reworded this sentence to "Nevertheless, the common occurrence of alpine meadows in the areas between talus and stream channels within many alpine watersheds (see Figure 5 in Caballero et al., 2002) suggests..."

Technical comments:

8.We have followed advice from both reviewers (see response to reviewer 1) and have split Figure 2 into a new Figure 2 and Figure 3.

HESSD

7, C722–C732, 2010

Revised Figure Captions

Figure 1. Topographic map of the Opabin watershed showing Opabin Creek (gray solid line), major lakes (gray bodies), a glacier (stippled), and the automatic weather station (AWS). Black square indicates the location of the hydrological and geophysical surveys on the talus-meadow complex shown in Figures 2 and 3. Contour interval is 50 m. The insert shows the site location in North America.

Figure 2. Three-dimensional photo-draped digital elevation model of the talus-meadow complex (outlined by dashed line). White line - small stream that flows intermittently across the meadow and drains into a neighboring gully. No vertical exaggeration. Coordinates are in UTM grid.

Figure 3. (a) Contour map of the same region shown in Figure 2 with location of the five GPR profiles (red lines), centers of five common-midpoint (CMP) GPR profiles (red circles), four ERT profiles (green lines), and the shot and receiver array of the seismic refraction profile (dark blue line). Yellow body shows the area of the alpine meadow and gray body the area of the talus cones. Also shown are the locations of four piezometers (black circles), the monitoring weir (triangle), and the excavated soil pit (square). Blue dotted line - course of the small stream. Contour elevations are in meters. (b) Photo of the talus-meadow complex taken from the top of profile GPR1/ERT1 and looking to the southwest. Also shown are the locations of piezometers P1-P4 and profile GPR2/ERT2.

Figure 4. Processed GPR cross-sections from profiles (a) GPR1 and (b) GPR2. Profile locations are shown in Figure 3a. Block arrows show where the two lines intersect. Three zones with different surface characteristics are demarcated: meadow, unvegetated talus and vegetated talus. The dots in (b) mark the projected locations of the center of the CMP1 GPR profile, piezometer P1 and the cluster of piezometers P2-P4 onto profile GPR2. AW and GW in (b) indicate the airwave and groundwave phases, respectively.

HESSD

7, C722–C732, 2010

Figure 5. (a) GPR data from CMP1, which was recorded using 50 MHz antennas (location shown in Figure 3a). Solid line shows the linear moveout of the picked airwave phase (Va); dashed lines show the linear moveout of a slow groundwave phase attributed to a thin soil layer (Vg1), and the normal moveout of a subsurface reflection (Vr1); dotted line shows the linear moveout of a second fast groundwave phase attributed to a substrate of bedrock underlying the meadow (Vg2). (b) Corresponding semblance plot for which warmer colours represent higher values. Circle defines the normal moveout velocity calculated for picked reflection Vr1 shown in (a).

Figure 6. As for Figure 4, but with the corresponding inverted electrical resistivity tomograms ERT1 and ERT 2 overlain onto the GPR cross-sections. ERT model cells with DOI values >0.2 are not plotted (see text for explanation).

Figure 7. Example shot gather recorded from shot point 5 (SP5), which was located on a talus deposit (the shot point location is shown on the seismic tomogram in Figure 8). Circles are observed first-break picks and squares are calculated travel-times from the inverted velocity model.

Figure 8. (a) Inverted p-wave velocity tomogram for the seismic refraction profile (location shown in Figure 3a). Shot-receiver raypaths calculated for the model are plotted as black lines. Shot gather data from shot point SP5 are shown in Figure 7. (b) The same p-wave velocity tomogram as shown in (a) but plotted as a transparent overlay onto the corresponding cross-section for profile GPR1. Regions of the model that are not traversed by the raypaths shown in (a) are not plotted.

Figure 9. Contoured maps of (a) meadow topography from 2-m LIDAR DEM, (b) subsurface bedrock topography produced by interpolating bedrock picks made on ERT and GPR profiles, and (c) depth to bedrock produced by differencing (a) and (b). Dotted line – surface stream channel; circles – piezometers P1-P4 and the center of the CMP1 GPR profile; triangle – monitoring weir; square – excavated soil pit.

Figure 10. Hydrological data for June-September, 2008. (a) Daily precipitation. (b)

HESSD

7, C722–C732, 2010

Elevation (above mean sea level) of the water level in piezometer P4. Dashed line indicates the ground surface at this location. (c) Discharge measured at the weir. See Figures 3a and 9 for the location of P4 and the weir.

Figure 11. Schematic diagram showing the internal structure and groundwater and surface water flow pathways in the talus-meadow complex.

Interactive comment on Hydrol. Earth Syst. Sci. Discuss., 7, 1535, 2010.

Figure 5

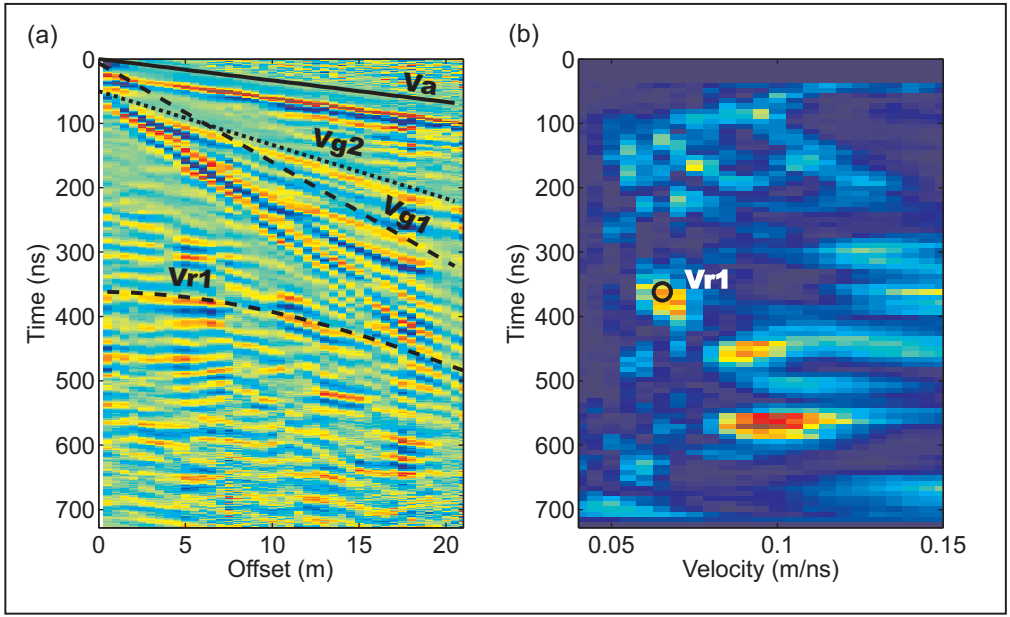

Fig. 1. Figure 5

HESSD
7, C722–C732, 2010

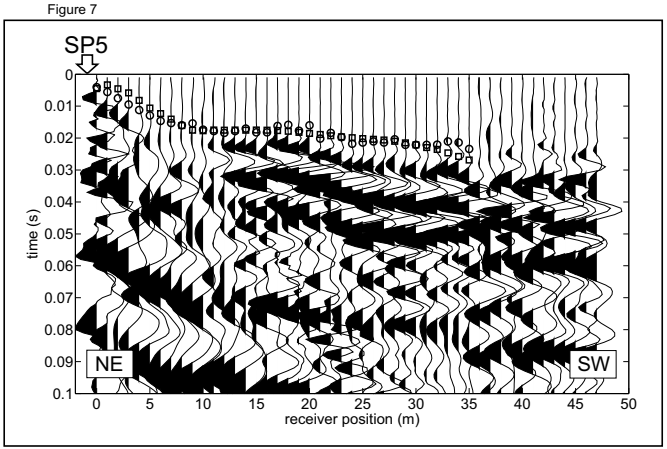

Fig. 2. Figure 7

HESSD
7, C722–C732, 2010

Interactive Comment

Figure 6

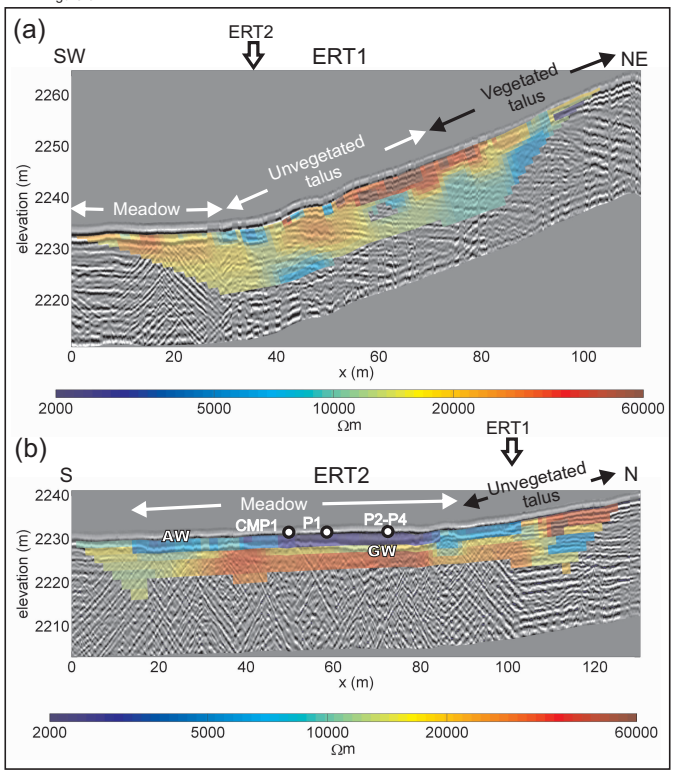

Fig. 3. Figure 6

HESSD
7, C722–C732, 2010

Full Screen / Esc
Printer-friendly Version
Interactive Discussion
Discussion Paper